

## The Impact of Sea-Ice Drift and Ocean Circulation on Dispersal of Toothfish Eggs and Juveniles in the Ross Gyre and Amundsen Sea

Erik Behrens<sup>1</sup> , Matt Pinkerton<sup>1</sup> , Steve Parker<sup>1</sup> , Graham Rickard<sup>1</sup> , and Charine Collins<sup>1</sup> 

<sup>1</sup>National Institute of Water and Atmospheric Research, Wellington, New Zealand

### Key Points:

- Particles drift from the northern Ross Sea and Southeast Pacific Basin to the continental shelf break as a part of the Ross Gyre circulation
- Recruitment success is 70% lower for particles which drift with sea-ice, but particles reach the shelf break around 100 days earlier
- Sea-ice advected particles are carried away from the shelf break, in the north-eastern Ross Gyre during the second winter season

### Correspondence to:

E. Behrens,  
[erik.behrens@niwa.co.nz](mailto:erik.behrens@niwa.co.nz)

### Citation:

Behrens, E., Pinkerton, M., Parker, S., Rickard, G., & Collins, C. (2021). The impact of sea-ice drift and ocean circulation on dispersal of toothfish eggs and juveniles in the Ross Gyre and Amundsen Sea. *Journal of Geophysical Research: Oceans*, 126, e2021JC017329. <https://doi.org/10.1029/2021JC017329>

Received 2 MAR 2021  
Accepted 7 SEP 2021

**Abstract** Knowledge about the early life history of Antarctic toothfish (*Dissostichus mawsoni*) is still incomplete, particularly on the spatial and temporal extent of spawning and the subsequent transport of eggs, larvae, and juveniles from the offshore spawning areas to the continental shelf. This study used a high-resolution hydrodynamic model to investigate the impact of ocean circulation and sea-ice drift on the dispersal of eggs, larvae, and juvenile Antarctic toothfish. The virtual eggs were released on seamounts of the Pacific-Antarctic ridge in the Ross Gyre and advected using hydrodynamical model data. Particles were seeded annually over the years 2002–2016 and tracked for 3 years after their release. Recruitment success was evaluated based on the number of juveniles that reached known coastal recruitment areas, between the eastern Ross and Amundsen Seas, within 3 years. Sensitivities to certain juvenile behaviors were explored and showed that recruitment success was reduced by around 70% if juveniles drifted with sea-ice during the second winter season as this carried them into the open ocean away from the shelf region. Recruitment success increased during the second winter season if juveniles were entrained in the Ross Gyre circulation or if they actively swam toward the shelf. These modeling results suggest that the ecological advantage of sea-ice association in the early life cycle of toothfish diminishes as they grow, promoting a behavior change during their second winter.

**Plain Language Summary** The Antarctic toothfish, *Dissostichus mawsoni*, is a large, commercially harvested fish in the Southern Ocean. Hypotheses have been put forward around the importance of sea-ice for their early life stage, which this study investigates. These fish lay buoyant eggs in the water column during winter season. Spawning locations have been identified around seamounts in the Ross Gyre. After spawning the buoyant eggs float to the surface where they drift with sea-ice until they hatch. After hatching the juvenile fish are hypothesized to travel from the Northern Ross Gyre region to the continental shelf break between the eastern Ross and Amundsen Seas within 2–3 years. In this study, we investigate how ocean currents and sea-ice drift influence their journey by using data from a high-resolution ocean model. Simulations with different particle behaviors reveal that their recruitment success is around 70% lower if juveniles would continue to drift with sea-ice instead of following ocean currents as juveniles. In particular, the modeled sea-ice drift during the second winter season carries many juveniles away from the shelf break. Results suggest that the advantage of sea-ice, providing food and shelter, diminishes as toothfish grow.

## 1. Introduction

Antarctic toothfish (*Dissostichus mawsoni*) is one of the few commercially exploited notothenioid species endemic to the seas around Antarctica. In the northern Ross Sea region (Figures 1a and 1b), it spawns on bathymetric features, such as seamounts and ridges during winter between early July and late August (Han- chet et al., 2008, 2015; Parker et al., 2019, 2021). Spawning and spent fish have been observed spanning from 150°W to 150°E longitude at latitudes near 65°S (Parker et al., 2019), while juveniles (50–100 cm size class) are abundant on the shelf and slope between the Ross and Amundsen Sea. However, much of the adult population is likely further south along the continental slope and under sea-ice during winter. The exact geographic distribution of depths of spawning of *D. mawsoni* is still unknown. Based on the observations from the Ross and Amundsen Sea, and from the South Sandwich Islands, *D. mawsoni* likely spawns in the Ross

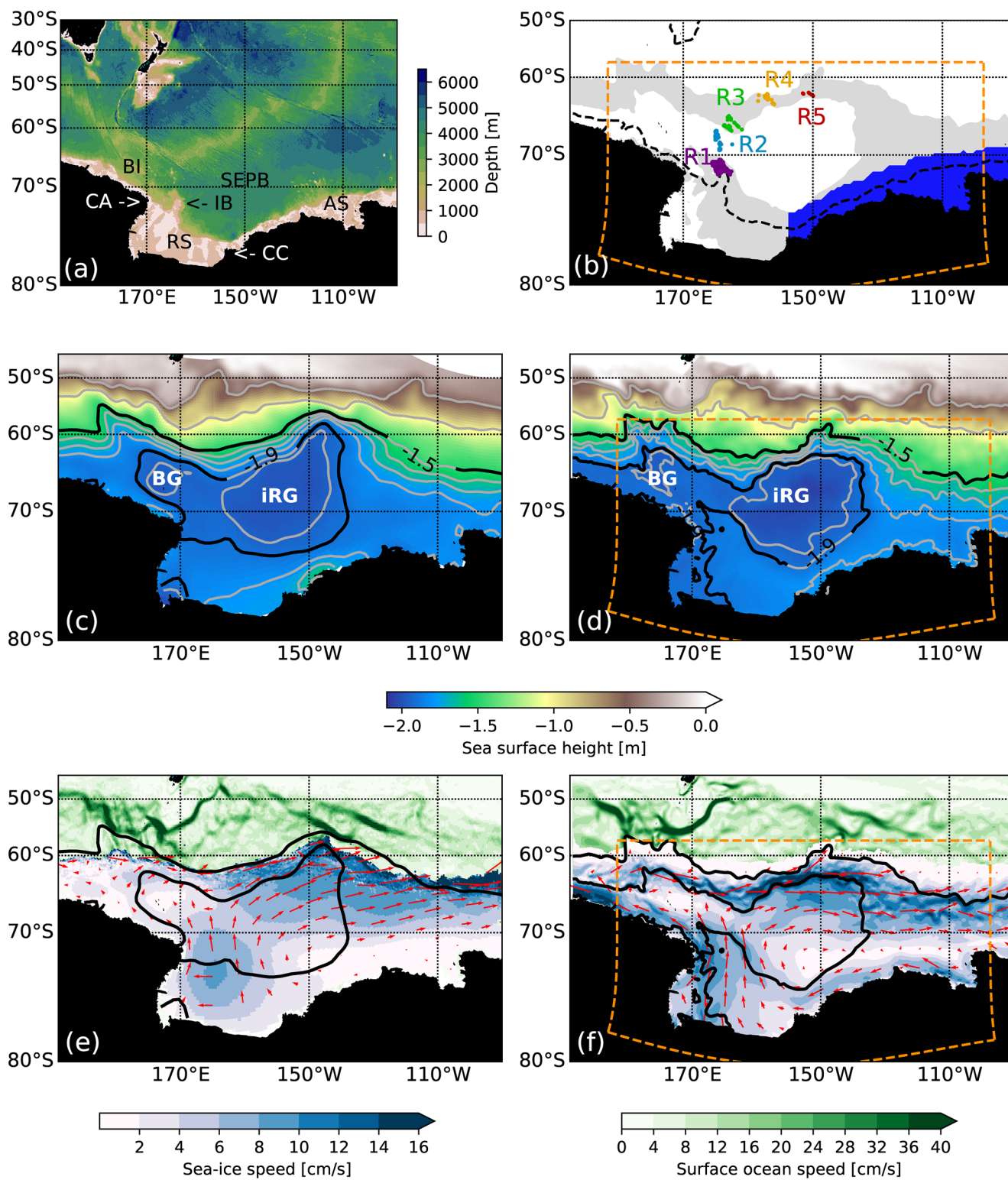


Figure 1.

Sea region, the region between Cape Adare and Cape Colbeck (Orsi & Wiederwohl, 2009), and in the Southeast Pacific Basin at depths of 1,000–2,000 m (Parker & Di Blasi, 2020; Parker et al., 2019; Roberts, 2012).

The Southeast Pacific Basin extends to the north of the Ross Sea into the Southern Ocean (Gouretski, 1999). The circulation in the Southeast Pacific Basin is characterized by the wind-driven cyclonic Ross Gyre, which extends from 160°E to 140°W and is largely restricted to the deep (>4,000 m) western region of the Southeast Pacific Basin (Carter et al., 2008). The Ross Gyre comprises the Antarctic Circumpolar Current to the north and the Antarctic margin, including the narrow, westward flowing Antarctic Slope Current to the south (Roach & Speer, 2019). The Antarctic Slope Current encircles the Antarctic continental shelf with sustained along-slope velocities of 10–30 cm/s (Thompson et al., 2018). The Ross Gyre can be divided into two cyclonic gyres (Figure 1c): the main, central Ross Gyre, and the Balleny Gyre, a secondary gyre centered on the Balleny Islands (Armitage et al., 2018).

The incubation time of *D. mawsoni* eggs as well as the period of passive drift is also not known precisely, largely due to the lack of winter plankton samples from the region. Nevertheless, hatching dates for *D. mawsoni* were estimated (La Mesa, 2007) from juvenile specimens collected around the South Shetland Islands by counting micro-increments between presumed hatching checks and sampling date identified in the core region of sagittal otoliths. Using this technique, it was estimated that hatching of *D. mawsoni* eggs takes place between November and February with a peak in December. Combined with developmental information from *D. eleginoides* (Mujica et al., 2016), a winter spawning period followed by a 3–4 months incubation and larval period in early spring is likely in the Ross Sea, Southeast Pacific Basin, and Amundsen Sea regions (Hanchet et al., 2008; Parker et al., 2019). The larval period is expected to be short (a few weeks) before an extended pelagic feeding phase as juveniles. Based on the lack of demersal juveniles smaller than 30 cm, it was hypothesized that *D. mawsoni* juveniles are likely to spend 1–2 years living in the plankton (Hanchet et al., 2008). It is likely that swimming abilities of larval and juvenile toothfish would increase during this period (Hanchet et al., 2008). Although no studies have been conducted linking toothfish juveniles and sea-ice, an association has been hypothesized based on the strongly buoyant eggs, timing of spawning, and likely locations of spawning (Parker et al., 2021).

Based on a combination of biological data, spatial distribution data, and Lagrangian particle tracking using hydrodynamical data from Hi-GEM (Shaffrey et al., 2009), a previous modeling study concluded that adult Antarctic toothfish move northwards from the Ross Sea to spawn on the banks and ridges of the Pacific-Antarctic Ridge during austral winter and spring (Hanchet et al., 2008). The Lagrangian particle tracking simulations suggest that the pathways and destination of juveniles depend on the exact spawning location and depth of transport (Ashford et al., 2012; Hanchet et al., 2008). The findings led to the hypothesis that eggs, larvae, and juveniles entrained in the Ross Sea gyres are transported eastwards and then southwards within the eastern Ross Gyre to settle out along the continental shelf and slope between the eastern Ross Sea and Amundsen Sea. Eggs from some possible spawning areas may be transported westward, from the Iselin Bank and seamounts north of it, to settle in the western Ross Sea, around the Balleny Islands, and the adjacent Antarctic continental shelf. In the hypothesized life cycle, the juveniles, once demersal, move back toward the northern Ross Sea shelf as they grow, eventually moving into deeper water as they mature over the ensuing decade (Hanchet et al., 2008).

In the present study, a series of Lagrangian particle tracking simulations based on ocean and sea-ice velocities obtained from a high-resolution ocean model hindcast is used to determine the pathways of particles

**Figure 1.** (a) Ocean bathymetry shown by the color shading over the Southwest Pacific Ocean. Locations of Cape Adare (CA), Balleny Islands (BI), Ross Sea (RS), Iselin Bank (IB), Southeast Pacific Basin (SEPB), Cape Colbeck (CC), and Amundsen Sea (AS) have been labeled. (b) Particles were seeded in five clusters (R1–R5) located in the western and northern Ross Gyre illustrated by modeled (2011–2016) sea surface height (gray area) between  $-1.9$  and  $-1.5$  m. The 1,000 m isobath of the continental shelf is shown by the black dashed contour line and the target region is indicated by the blue shaded polygon. Mean (2011–2016) sea surface height from (c) Cryosat and (d) ROAM15 are shown in color and gray contours (interval is 0.1 m). The  $-1.9$  and  $-1.5$  m contour lines have been highlighted in black for a better comparison between observations and model results. Two inner gyres, the Balleny Gyre (BG) and the inner Ross Gyre (iRG), are contained within the Ross Gyre. The dashed orange line in (b), (d), and (f) illustrates the boundaries of the high-resolution nest ( $1^\circ/15^\circ$ ) within the  $1^\circ/5^\circ$  nest which covers the Southwest Pacific. Mean June–September (2010–2017) sea-ice motion shown by the blue color shading from (e) Pathfinder satellite product and (f) ROAM15 in cm/s. Every 10th or 30th velocity vector is drawn for Pathfinder and ROAM15, respectively. The green shading in (e) and (f) represents mean (2010–2017) surface ocean speeds from satellites (Copernicus Marine Services) and ROAM15, respectively. Model data outside of the high-resolution ( $1^\circ/15^\circ$ ) region is based on data from the  $1^\circ/5^\circ$  southwest Pacific nest. The black contour lines show the highlighted sea-surface height contours from (c) and (d) to illustrate the Ross Gyre.

from five spawning regions within the Ross Gyre (Figure 1b) under different advection schemes, which mimic different hypothetical juvenile behaviors. The present study builds on and expands the previous work by investigating how certain juvenile behaviors and spawning regions influence particle trajectories and recruitment success using empirical data on buoyancy and timing of spawning (Parker et al., 2019, 2021). The various advection schemes were designed to explore the impact of ocean circulation and sea-ice drift as well as various biological strategies of toothfish (i.e., active swimming and diel vertical migration [DVM]) on the trajectories and variability in recruitment success of particles in reaching the “target region.” The main aim of this study is to explore how certain juvenile behaviors impact the particle trajectory, travel times, and overall recruitment success, to better understand the likely toothfish behavior during the juvenile period. Information about the spatial distribution of the population and the factors that affect recruitment are needed for management of this species in the Ross Sea and around the Antarctic Continent.

This article is structured as follows. Section 2 describes the model, advection schemes, and provides details around the diagnostics deployed in this article. Section 3 presents the results for particle trajectories, recruitment success rates, and travel time. Section 4 provides a discussion and conclusion of this article.

## 2. Methods

### 2.1. Model Setup

This Lagrangian dispersal study uses ocean and sea-ice data from a high-resolution ocean model hindcast. The ocean model is based on Nucleus for European Modeling of the Ocean (NEMO, Madec et al., 2017) version 3.6 and is fully coupled to the Louvain-la-Neuve Sea Ice Model (LIM 2, Fichefet & Maqueda, 1997) sea-ice model. A hindcast was generated for the period of 1958–2019 using atmospheric boundary conditions from JRA-55-DO v1.3 (Tsuji et al., 2018). The oceanic model grid is based on a global eORCA1 configuration, which has also been used for New Zealand’s Earth System Model (Behrens et al., 2020) and recent scientific studies to investigate marine heat waves in the Tasman Sea (Behrens et al., 2019). In this global non-eddy resolving grid an eddy-permitting ( $1^\circ/5^\circ$ , first nest) nested grid, spanning the Southwest Pacific between  $130^\circ\text{E}$ – $86^\circ\text{W}$  and  $81^\circ\text{S}$ – $25^\circ\text{S}$ , was embedded using the Adaptive Grid Refinement in Fortran (AGRIF, Debreu et al., 2008) nesting capabilities of NEMO.

To get to eddy resolving scales, a second nest, with a resolution of  $1^\circ/15^\circ$ , was embedded inside the first nest. This second nest, hereafter called ROAM15 (“Ross Amundsen Sea  $1^\circ/15^\circ$ ”), spans the Ross and Amundsen Sea between  $143^\circ\text{E}$ – $95^\circ\text{W}$  and  $80^\circ\text{S}$ – $57^\circ\text{S}$  (Figure 1). The nests and global model are coupled via a two-way nesting scheme and share the same vertical model grid with 75 vertical  $z$ -levels. The top level is 1 m thick, while the thickness increases to around 200 m below depths of 4,000 m. A partial cell parameterization (Barnier et al., 2006) was applied to improve the representation of the bottom topography and overflows. The timestep for the global model is 30 min but is reduced to 10 and 5 min for the Southwest Pacific and ROAM15 nests, respectively. Viscosity varies between  $1 \times 10^4 \text{ m}^2/\text{s}$  (Laplacian),  $5 \times 10^{10} \text{ m}^2/\text{s}$  (bi-Laplacian), and  $1 \times 10^9 \text{ m}^2/\text{s}$  (bi-Laplacian) for the global eORCA1, the Southwest Pacific, and ROAM15 nests, respectively. Horizontal lateral Laplacian diffusivity for tracer was set to 1,000, 200, and  $66 \text{ m}^2/\text{s}$ , respectively.

The hindcast was started from rest with climatological values for temperature and salinity based on EN4 (Good et al., 2013) fields generated over the period 1995–2014. Ice-shelf cavities were not explicitly simulated but meltwater fluxes were prescribed at the front of the ice-shelf edge and freshwater entered at the ocean surface. Due to the incompatibility of the Lagrangian iceberg scheme with AGRIF, meltwater fluxes from icebergs were prescribed, based on a climatology of a hindcast without AGRIF nests. Tidal flows have not been included in this model setup, while the tidal mixing has been taken into account.

### 2.2. Model Evaluation

Due to the dominance of sea-ice in the Ross and Amundsen Seas, winter observations are sparse or come with caveats reducing the ability to use them for model validation. However, progress has been made to produce satellite derived dataset allowing insights into the ocean dynamics of this region. Sea surface height characterizes the near-surface ocean circulation, represented by gradients in the sea surface height, and therefore can be used to visualize the Ross Sea gyre circulation (Armitage et al., 2018; Behrens et al., 2016; Kwok &

Morison, 2015; Meijers, 2014). Under idealized conditions particles would follow the sea surface height contour lines which can be interpreted as particles streamlines (Sokolov & Rintoul, 2009). Here we used the CryoSat-2 based product provided by Ron Kwok (<https://swot.jpl.nasa.gov/documents/1541/?list=projects>) which detects sea surface height in leads in the sea-ice pack and covers the period 2011–2016 (Kwok & Morison, 2015). In addition to the satellite product for sea-surface height, sea-ice velocities from the Pathfinder mission (<https://nsidc.org/data/NSIDC-0116>) were used for model validation.

The upper-ocean circulation in the northern Ross Sea is dominated by the Antarctic Slope Current, which forms the southern boundary of the cyclonic Ross Gyre. The Ross Gyre is bounded in the north by the Antarctic Circumpolar Current. Strong flows of the Antarctic Circumpolar Current are reflected in this region by densely packed sea surface height contour lines. The Ross Gyre is characterized by lower sea-surface height values and is clearly visible in the CryoSat-2 sea-surface height product (Figure 1c). The Ross Gyre comprises two cyclonic inner gyres, an inner “Balleny Gyre” in the north-western part, and an “inner Ross Gyre,” which occupies the eastern part. Both gyre centers only show very small changes in sea surface height, which indicates little flow compared to the outer regions of the gyre, where sea surface height gradient is larger. In the remainder of the manuscript, we use the term Ross Gyre to describe the overall Ross Gyre circulation, which includes both inner gyres.

The modeled sea surface height pattern shows similar patterns to the observations (Figure 1d). The  $-1.9$  m contour is used to illustrate the larger Ross Gyre. Note, that the  $-1.9$  m contour does not reflect the Ross Gyre boundary. In general, the  $-1.9$  m contour of the modeled Ross Gyre agrees well with the observations but expands too far south in the western Ross Sea and along the Oates Land coast, whereas the observed contour only touches the Antarctic Coast near Cape Adare. In addition, the modeled Ross Gyre does not extend far enough into the Southern Ocean at the north eastern boundary as suggested by the observations. Factors which potentially contribute to this discrepancy are the different horizontal resolutions of the satellite product ( $\sim 25$  km) and the model ( $< 3$  km) as well as the different reference levels, a WGS84 ellipsoid for CryoSat-2 and a sphere for the model. However, the good alignment of contour lines over the wider region into the Southern Ocean between both data sources indicates that the model is able to represent the large-scale circulation in agreement with observations. The overall Ross Gyre transport, based on the barotropic streamfunction in the Ross Gyre center, is 27.8 Sv, which is within the range of estimates of 20–30 Sv (Dotto et al., 2018; Roach & Speer, 2019).

The satellite derived wintertime (June–September) sea-ice drift shows a northward drift over the western Ross Gyre (Figure 1e). East of  $170^{\circ}\text{W}$  and north of around  $70^{\circ}\text{S}$  sea-ice is deflected to the east due to the prevailing westerly winds. The sea-ice drift east of  $150^{\circ}\text{W}$  is perpendicular to the  $-1.9$  m sea surface height contour and causes sea-ice to be carried across the Ross Gyre into the Southern Ocean. The model results show the same characteristics but with more detailed structure due to the finer model grid ( $\sim 3$  km; Figure 1f) compared to the satellite product (25 km) and resolved mesoscale activity. In the northeastern Ross Gyre, the modeled sea-ice motion is more zonally directed than the observations, which means modeled sea-ice is not being carried as far north as the observations suggest. In addition, the model shows stronger sea-ice flow along the coast and within the model’s energetic Antarctic Slope Current, which is not present in the satellite derived sea-ice drift. Reasons for the larger sea-ice flows in this region could be a case of a too strong coupling between ocean momentum and sea-ice drift in the model. Overall, the model appears to effectively capture the large-scale sea-ice drift. North of the sea-ice covered region the imprint of the easterly flow of the Antarctic Circumpolar Current (green shading) is present. The model sea surface ocean speed pattern is very similar to that obtained from satellites (<https://marine.copernicus.eu/>, SEALEVEL\_GLO\_PHY\_L4\_REP\_OBSERVATIONS\_008\_047), suggesting a good fit between observed and modeled surface ocean currents.

### 2.3. Particle Release Strategy and Tracking

Particles were seeded over five distinct regions within the Ross Gyre where mature female toothfish are prevalent and likely spawn (R1–R5, Figure 1b; Hanchet et al., 2015). These regions are associated with seamounts in the Southeast Pacific Basin and the shelf break around the Iselin Bank area (seeding region R1). Regions R3–R5 are within the sea surface height range that connects the northern rim of the Ross Gyre with the shelf of Antarctica (gray shaded area). Sea-ice drift from the southern spawning regions R1 and R2 will

transport the eggs north into the Ross Gyre boundary into the sea level range which would connect them with the Antarctic shelf and provides a potential pathway. Furthermore, R1 and R2 are regions with high toothfish abundance and where adolescent and adult fish are observed (Hanchet et al., 2015). Empirical information on the timing of spawning or depth of transport was absent and plausible values were determined by finding spawning times and locations that resulted in successful transport to putative recruitment areas (Ashford et al., 2012; Hanchet et al., 2008).

*Parcels* (Delandmeter & van Sebille, 2019), an open-source Python based Application Programming Interface for Lagrangian ocean analysis, was used to simulate the transport of virtual toothfish eggs, larvae, and juveniles using environmental variables (ocean current velocities and sea-ice motion) from ROAM15. *Parcels* was chosen as it allows for flexible and modular particle advection and supports the NEMO ocean grids.

Every day between the 15th July and 15th September—the likely spawning season of toothfish in the region (Parker et al., 2019)—411 particles spanning the five spawning regions were released and advected for up to 3 years using the ocean and sea-ice fields from ROAM15. The number of particles released at each seeding location was scaled according to the size of the seeding location. This seeding procedure, with a total of 25,893 particles for each year, was repeated for every year from 2002 to 2016. The particle seeding was stopped in 2016 to allow for a 3-year particle advection. If particles reached the model domain boundary during that timeframe the tracking was stopped, and particles removed from the point in time. Particles were advected using five-daily averaged hydrodynamic fields from ROAM15 and the locations and velocities of each particle were archived as daily snapshots.

#### 2.4. Particle Advection Schemes

The general particle advection is based on a Runge-Kutta fourth order advection with a timestep of 1 h, following previous studies with a similar setup (Daher et al., 2020). Five variations to this general advection scheme were implemented to test the sensitivity of dispersal to assumptions about sea-ice advection (SA), ocean advection (OA), advection at depth, DVM, and active southward movement/velocity (SV) toward the Antarctic shelf (Figure 2).

Particles were seeded 50 m above the seamounts, which were typically at depths of 1,300 m, and floated to the surface with an average vertical velocity of 0.311 cm/s consistent with recent measurements of egg buoyancy (Parker et al., 2021). During the ascent through the water column particles were advected with the ocean currents. After 3.5–7.5 days the particles reach the surface. If the particles then encounter sea-ice they move with the sea-ice, otherwise they are advected with the ocean velocity in the surface layer (Figure 2a), which is 1 m thick in ROAM15. The toothfish eggs are assumed to hatch into non-feeding and passive larvae 100 days after spawning. Then, after 2 weeks, the larvae become motile and feeding juveniles (Mujica et al., 2016). From this point of a transition from non-motile larvae to motile juveniles, a set of nine advection schemes (some with additional variations) are applied for the remaining 995 days.

The nine advection schemes are graphically illustrated in Figure 2 with the variations applied to some of the advection schemes. Below follows a brief description of the nine advection schemes:

1. Particles subjected to the SA scheme (Figure 2b), were transported with sea-ice if it was encountered, otherwise they drifted with the ocean surface velocity.
2. The SA or advection at depth scheme (Figure 2c), 200 and 400 m, follows: (1) but if no sea-ice was present the juveniles moved to a prescribed depth (the deep scattering layer for a food source and protection from predators) instead of staying at the surface and ocean velocities at this depth were used for the particle advection. We used depths of 200 or 400 m here to explore how variations of ocean currents with depth impact the dispersal. Particles move within 1-h timestep between sea-ice and the prescribed depth, which effectively results in a 5 or 11 cm/s migration velocity for 200 and 400 m, respectively.
3. The SA or advection at depth and 12-h DVM scheme (Figure 2d), 200 and 400 m DVM, is similar to (2) but instead of staying at a fixed depth the juveniles performed a DVM between the prescribed depth and the surface when no sea-ice was present. Toothfish vertical migration velocities are still unknown and thus this advection scheme was set-up so that particles moved between the surface and prescribed depth within 1-h. This effectively results in a 5 or 11 cm/s migration velocity for 200 and 400 m, respectively. Similar to (2), a maximum depth of 200 or 400 m was used.

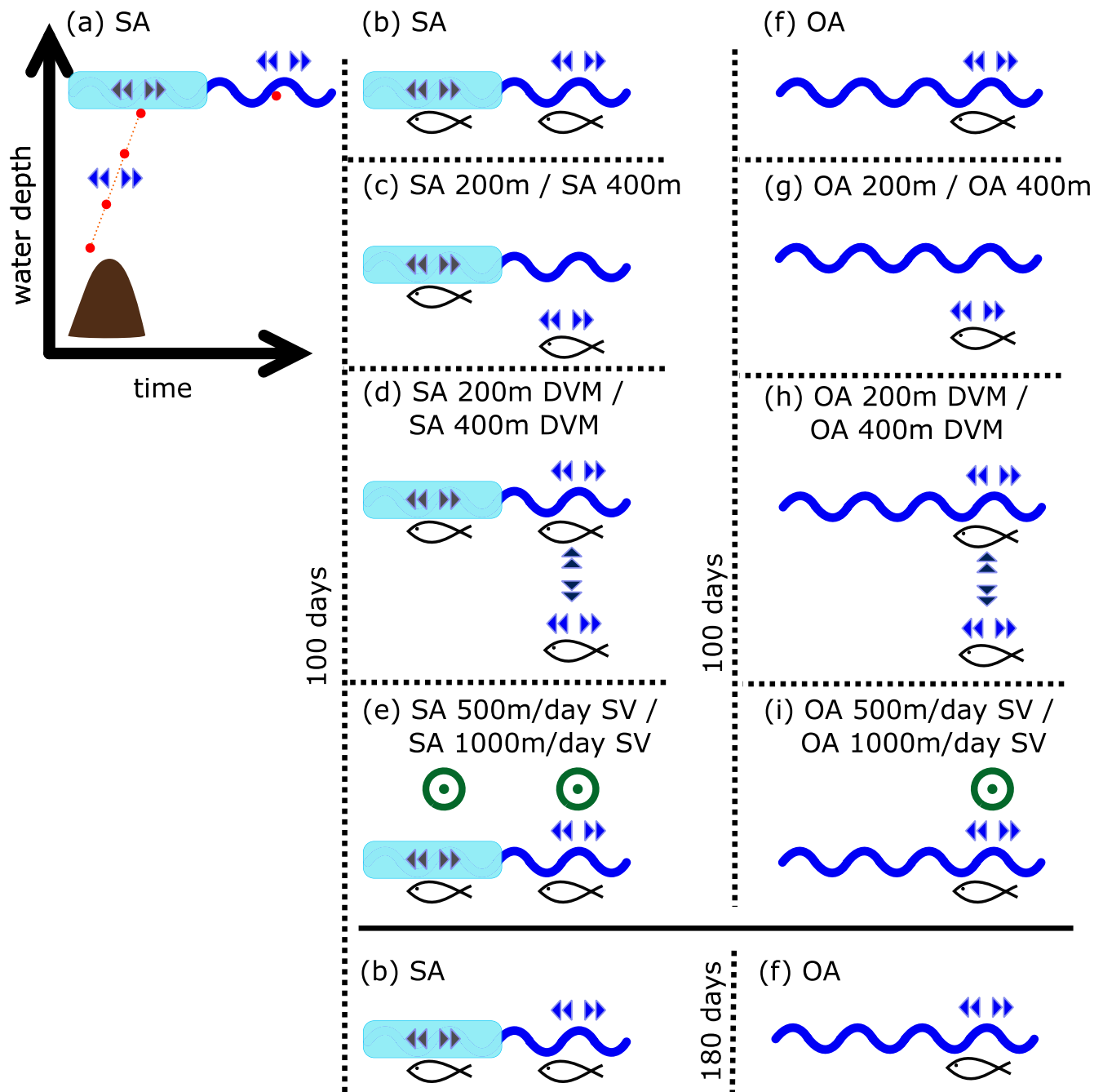


**Figure 2.** Advection schemes for the Lagrangian particle tracking: Every particle (red dots) is seeded 50 m above the sea floor at sites R1–R5. (a) Particles ascend to the surface with a vertical velocity of 0.311 cm/s and are advected with ocean currents until they reach the surface. When the particles have reached the surface the Sea-ice advection (SA) scheme is used. After hatching (100 days) each particle is assigned one specific advection scheme (b–i) for the remaining time. The ocean advection (OA) schemes are counter parts to the SA, where the presence of sea-ice is ignored. Diel vertical migration, labeled DVM, is where the juveniles migrated between the surface and a specific depth. Southward active swimming (SV) is indicated by the green circles with a dot in the middle. The SA 180 days advection scheme is illustrated at the bottom, where juveniles change their behavior from SA to OA after 180 days.

4. The SA with active southward swimming scheme (Figure 2e), hereafter SA southward velocity (SV) of 500 and 1,000 m/day, is similar to the advection scheme in (1) but an additional SV of either 500 or 1,000 m/day (based on assumed sustained swimming capabilities of juvenile toothfish) was applied to the particle velocities after hatching to simulate active swimming toward the Antarctic coast.

5. In the OA scheme (Figure 2f), the presence of sea-ice was ignored, and the particles were advected with the surface ocean velocities regardless of whether sea-ice was present or not.
6. The OA at depth scheme (Figure 2g) of 200 and 400 m, is the same as (5), however, particles were advected at a prescribed depth of 200 or 400 m. The particles moved between the surface and prescribed depths as in (2).
7. The OA at depth and DVM scheme (Figure 2h) of 200 and 400 m, is similar to (6) but instead of staying at a fixed depth the juveniles performed a 12-h DVM between either 200 or 400 m. The particles moved between the surface and prescribed depth as described in (3).
8. The OA at the surface with active southward swimming scheme (Figure 2i), 500 and 1,000 m, is similar to (5) but an additional southward motion of 500 or 1,000 m/day was applied to the particle velocities to simulate active swimming toward the Antarctic coast.
9. The SA until 180 days of spawning, is a special case to test the importance of sea-ice during the second winter season. After 180 days of SA (bottom of Figure 2) particles switch to OA for the remaining period.

The general lack of knowledge around the toothfish behavior after hatching motivated the above described advection schemes and seeks to explore how sensitive their recruitment success is to these different behaviors. The advection schemes which ignore sea-ice presence (OA) seeks to explore how sea-ice drift in general impacts the particle trajectories and recruitment success. As sea-ice cover might decline in a warmer climate in this region, the OA advection schemes provide some first insights on the impact of climate change on toothfish recruitment. The advection schemes where juveniles show a preference to a certain depth or perform a DVM are motivated by the assumption that toothfish near the surface without sea-ice would be more exposed to predators which is considered unfavorable and a reason to avoid the surface. However, currents at depth differ compared to the surface currents in magnitude and direction, which will have an impact on the particle's trajectory with unknown consequences for their recruitment success. The advection schemes which impose a southward swimming aim to explore juvenile toothfish's growing swimming potential to reach the Antarctic coast faster. That would decrease juvenile toothfish's exposure to open ocean predators. However, active swimming is physically demanding which could reduce the benefit of reaching the Antarctic coast earlier. The above schemes seek to explore how sea-ice drift versus ocean velocity affect the recruitment success.

The SA 180 days scheme was developed to test for the importance of sea-ice drift during the second winter season, when particles are found in the north eastern Ross Gyre, and sea-ice drift tends to carry particles away from the shelf break into the Southern Ocean. This scheme is very similar to OA, but the transition between SA and OA is not motivated by presumed hatching dates (100 days) but timed to align with the middle of summer (180 days). This is the period when sea-ice concentration is lowest, and particles should be transported by ocean currents.

### 2.5. Particle Separation, Diagnostics, and Target Region

For analysis, particles were separated into successful and unsuccessful particles. Successful particles were defined as particles which entered the target region within 3 years of being released. The target region has been defined as the stretch of ocean between the shelf and slope east of 155°W and 95°W and 100 km north of the 1,000 m isobath (and shown as the blue shaded polygon in Figure 1b), based on locations where the smallest demersal toothfish (~30 cm in length) have been observed (Hanchet et al., 2008). Although the areas around the Balleny Islands and west of Cape Adare have been identified as regions for settling, they have not been explored in this study due to the lack of information about both the adults and juveniles in these areas. Particles did not have to remain in the target region to be classified as successful. Particles which never entered the target region were identified as unsuccessful.

To illustrate the dispersal of all released particles, two-dimensional (longitude vs. latitude) particle probabilities were calculated to illustrate the overall path of particles and their spread. The daily particle location, binned onto a regular  $0.5^\circ \times 0.5^\circ$  grid over each 3-yr long simulation from 2002 to 2016, showed the total number of particles which passed through this grid box over the entire time. If particles remained in the same grid box over time or re-entered, they were counted again. This diagnostic was applied to successful and unsuccessful particles separately to illustrate differences in the specific pathways. Once particles have

entered the target region or left the model domain their locations were excluded from the calculations. Furthermore, the longitude where particles enter the target region was recorded to identify certain spatial recruitment preferences and longitude bins of  $0.5^\circ$  width were used for this diagnostic.

Mean trajectories were computed for the individual seeding regions R1–R5 for successful and unsuccessful particles to illustrate the individual pathways. Here, all particle locations for a certain day after spawning were averaged together to obtain a mean location. These daily mean locations form the mean particles trajectory for each seeding region. The particle spread increases with time which can result in mean locations which have never been occupied by any particle. We tried to reduce this unwanted representation by grouping similar particles together, by the same seeding location and by separating them in successful and unsuccessful particles. The latter leads to the largest bifurcation in the particle pathways. Particles which left the modeling domain were truncated from that point in time as well as particle locations after they have entered the target region.

The influx of particles into the target region was computed for each seeding region over time, providing the total number of particles which enter the target region every day. This metric also allows the particle age and the time of first arrival into the target region for a certain seeding region to be determined. In addition, the cumulative influx was computed over all seeding regions relative to the total number of successful particles.

### 3. Results

#### 3.1. Success Rate, Travel Times, and Seeding Location Dependency

The time-averaged (2002–2016) recruitment success rates of successful particles over all seeding regions (R1–R5) are shown in Figure 3a. There is a clear distinction in the success rates of particles which use sea-ice motion versus particles which ignore its presence (Figure 3a). Particles drifting with sea-ice and without any active southward swimming have a relatively low success rate ( $<8\%$ , gray bars) in reaching the Antarctic continental shelf within a period of 3 years. On the other hand ocean advected particles show success rates of  $12\%$ – $24\%$  (dark blue bars) suggesting a doubling to tripling of the success rate. The error bars (10th and 90th percentile) show that success rates can drop to values below  $1\%$  for individual years for SA schemes. For some years and seeding regions the recruitment success is intermittent (not shown).

SA combined with either advection at a fixed depth or DVM under ice free conditions has no obvious impact on the success rate and shows similar success rates to the SA schemes where particles stay at the surface. In contrast, simulations where an active swimming toward the Antarctic coast is incorporated show a significant increase in success rates. The mean success rate in these active swimming schemes increases from  $\sim 8\%$  to  $\sim 25\%$  with a swimming speed of  $500$  m/day and to nearly  $50\%$  if juveniles were to maintain a speed of  $1,000$  m/day after hatching. While the range increases in these simulations the trend toward higher success rates with increased southward swimming appears to be robust, with success rates only dropping below  $10\%$  for a few individual release years (2004, 2013, and 2015, not shown).

In the OA schemes, the recruitment success is not intermittent between years, but the range is larger than in the SA schemes. OA at a fixed depth results in a slight decrease in success rates ( $\sim 18\%$  and  $12\%$  for advection at  $200$  and  $400$  m, respectively), compared to the success rate of the ocean surface advection scheme ( $24\%$ ). The addition of DVM has no significant impact on the success rate and both simulations show recruitment success rates between  $24\%$  and  $21\%$  similar to the success rate of the ocean surface advection scheme. Comparable with the SA schemes, the OA schemes with active swimming toward the Antarctic coast have significantly higher success rates compared to the other OA schemes. A swim rate of  $500$  and  $1,000$  m/day increases the success rate to more than  $30\%$ . However, the success rate does not increase with increased swimming rates (the relationship is nonlinear).

In addition, the scheme where particles were subjected to SA for the first 180 days followed by OA for the remaining period (cyan bar) shows a success rate slightly higher ( $29\%$ ) than the recruitment success rate of the ocean surface advection scheme ( $24\%$ ). At the same time the range has increased from  $\pm 12\%$  to  $\pm 18\%$ , but results are very similar to the OA scheme. This suggests that the particle drift during the second winter seasons is important for the overall recruitment success rate.

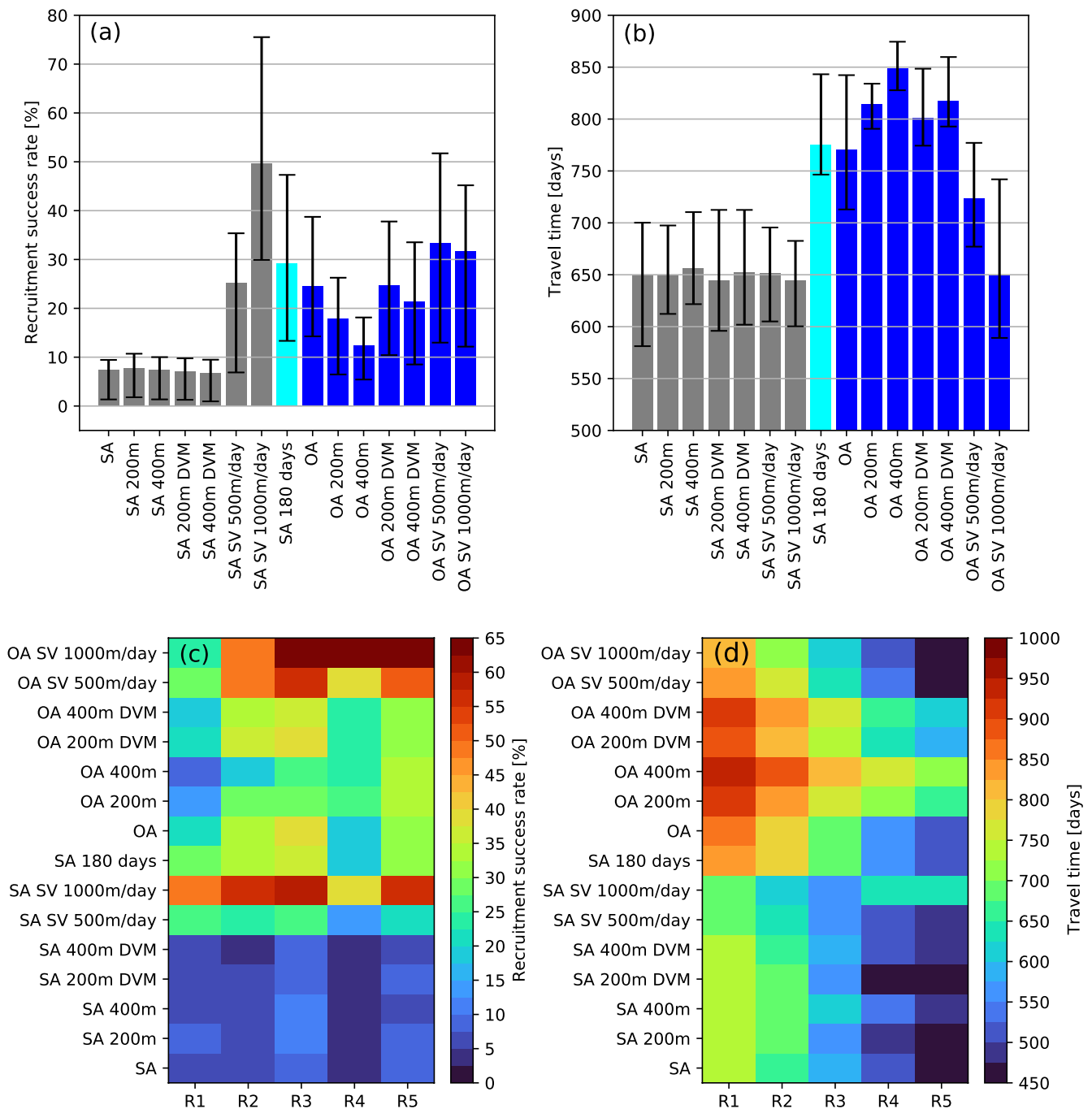


**Figure 3.** (a) Time-averaged (2002–2016) recruitment success rates: Fraction of particles seeded in regions R1–R5 that made their way into the target region (blue shaded region in Figure 1b) within 3 years. SA refers to sea-ice advected particles, while OA refers to ocean advected particles, SV to southward velocity, and DVM to diel vertical migration. (b) Time-averaged (2002–2016) travel times in days for successful particles. The gray bars show results for experiments which are based on SA while the blue bars are based on OA. The cyan bar is the SA 180 days simulation. Error bars show the 10th and 90th percentile for the yearly recruitment success rates over all seeding locations. Panels (c and d) show time-averaged (2002–2016) recruitment success rates and travel times of successful particles, respectively, from the different advection schemes in relation to the seeding locations (R1–R5).

The time-averaged (2002–2016) travel times for all successful particles from all seeding locations are shown in Figure 3b. Like with the recruitment success rate, there is a clear contrast in the travel times between SA schemes and OA schemes. Although the recruitment success rates for sea-ice advected particles are relatively low, they reach the Antarctic shelf 100–200 days earlier than the ocean advected particles. The

shorter travel times of particles subjected to the SA schemes apply regardless of the particle release location (Figure 3d). The shorter travel time of SA particles can be attributed to larger sea-ice velocities compared to the surface ocean velocities and a slightly more direct and shorter pathway toward the target region for successful particles.

The time-averaged (2002–2016) travel time for successful sea-ice advected particles is around 650 days with a range (10th–90th percentile) of around 100 days (Figure 3b). There is no clear travel time dependency among the different SA schemes, even for the schemes with active swimming that have higher recruitment success rates. The travel times for the OA schemes vary between 650 and 850 days. The range is reduced (<100 days except for OA) compared to the SA schemes. Particles subjected to OA at a fixed depth or performing a DVM take longer (>800 days) to reach the Antarctic shelf compared to all other advection schemes. The addition of active swimming toward the Antarctic coast shortens the travel time by around 50–130 days, compared to the ocean surface advection scheme. The travel time of the simulation where SA is applied for the first 180 days and OA for the remaining period (cyan bar) shows a travel time very similar to the surface OA schemes.

The results above summarize the trajectories for particles released over all seeding locations (R1–R5). A more detailed breakdown of recruitment success rates and travel times for the five individual seeding regions is provided in Figures 3c and 3d. For the SA schemes without active swimming, regions R3 and R5 show, in general, slightly higher (>7.5%) recruitment success rates compared to the other seeding regions. For SA at a fixed 200 m depth, higher recruitment success rates are also seen for R1. Irrespective of advection scheme, the “distance to the target region”—measured in terms of clockwise circulation around the inner Ross Gyre—is not the primary factor controlling the recruitment success rate. In other words, success rates of R5 are not necessarily higher than success rates of R1, which is further away from the target region. For the SA schemes with an active southward swimming, the recruitment success rates increase for all seeding regions, although not uniformly. With swimming speeds of 500 and 1,000 m/day, the increase in recruitment success rates is higher for R1 (by 200% and 700%) and R2 (by 150% and 750%) than for R3 (by 50% and 325%), R4 (by 50% and 400%), and R5 (by 30% and 360%), respectively. This demonstrates the non-linear nature of these spatial and temporal dependencies for the particle trajectory.

The OA schemes show higher recruitment success rates (>20%) for R2, R3, and R5, compared to R1 and R4. Similar to the SA schemes, the OA schemes with active swimming show a non-uniform increase in recruitment success rates. The increase in recruitment success rates for R4 (233% and 350%) and R5 (133% and 233%) are higher than for R1 (100% and 100%), R2 (100% and 75%), and R3 (100% and 100%) for swimming speeds of 500 and 1,000 m/day, respectively. For the SA schemes the regions R1 and R2, furthest in distance from the target region, show the largest increase in recruitment success rate while for the OA schemes the regions closer to the target region (R4 and R5) show a larger increase. The SA 180 days scheme shows very similar success rates to the OA scheme.

For the individual seeding locations (Figure 3d), a coherent increase in travel times with increasing distance from the target region is visible for all scenarios ( $R1 > R2 > R3 > R4 > R5$ ).

The travel times are relatively insensitive to the choice of the SA scheme. As seen in Figure 3b, the travel times of the OA schemes are more variable than those of the SA schemes. This is also evident for the individual seeding locations, which show a longer spread among the OA schemes. In the schemes with active southward swimming, the travel time reduced for all seeding locations except for R4 and R5 in the SA schemes.

### 3.2. Particle Probabilities and Mean Pathways

The daily recorded particle positions (2002–2018) for selected advection schemes were used to compute particle probabilities. The particle probabilities and average particle trajectories were computed for unsuccessful (Figure 4) and successful (Figure 5) particles separately. The particle probabilities are only presented for a subset of schemes, since the differences between the individual schemes are minor.

The unsuccessful particles in the three SA schemes (Figures 4a, 4d, and 4f) are zonally transported out of the influence of the Ross Gyre at a latitude of around 65°S, with a small number of particles circling in the

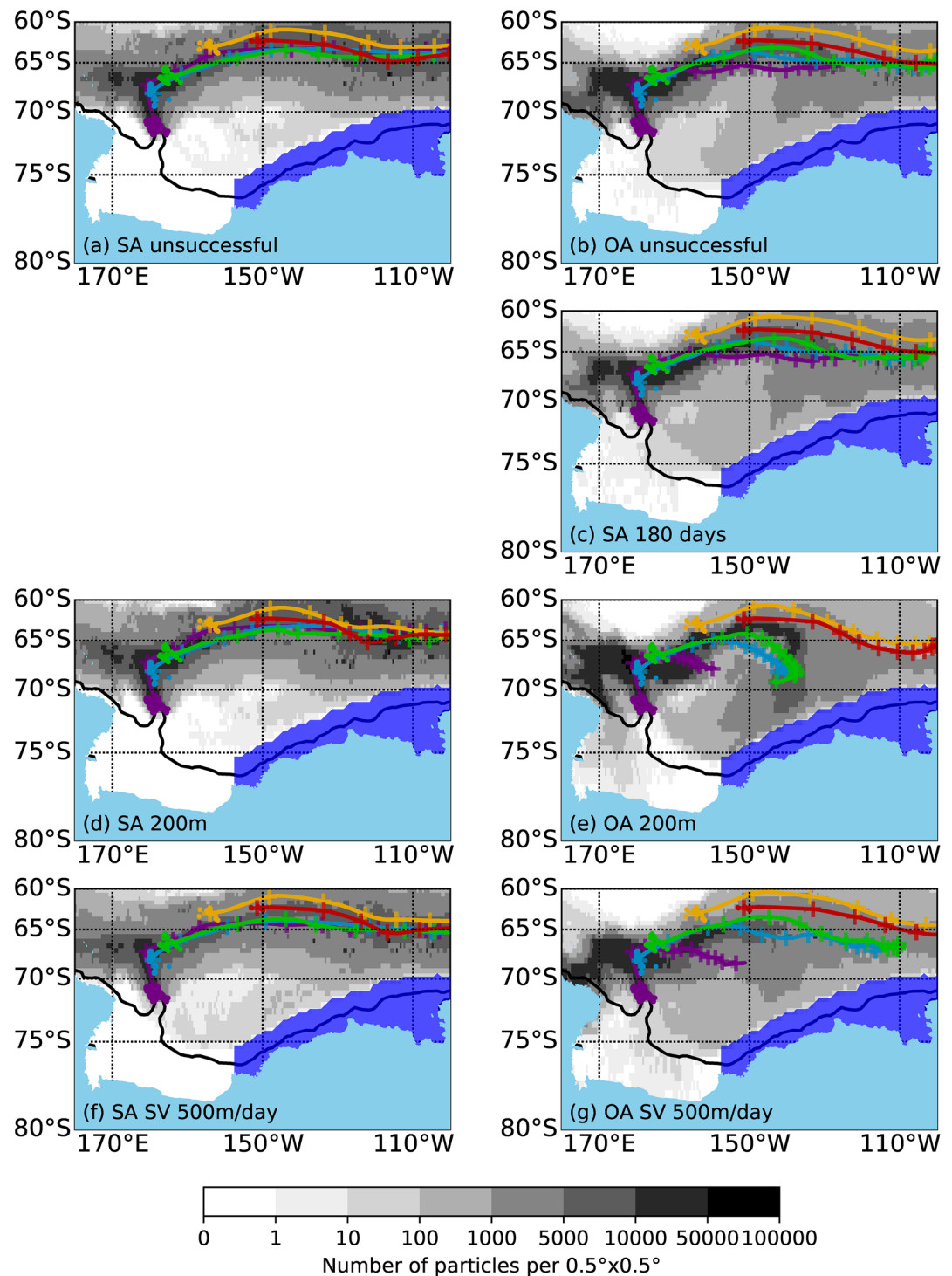


**Figure 4.** Particle probabilities (gray shading, release years 2002–2016) for unsuccessful particles from different advection schemes. Unsuccessful particles are defined as particles that fail to reach the target region (dark blue polygon) within 3 years. Note the non-linear scale. Solid lines represent the mean trajectories of the unsuccessful particles released from R1 (purple), R2 (light blue), R3 (green), R4 (orange), and R5 (red). (a) Sea-ice advection (SA); (b) Ocean advection (OA); (c) SA 180 days; (d) SA or OA at depth (200 m); (e) OA at depth (200 m); (f) SA + SV (500 m/day); (g) OA + SV (500 m/day). The black contour line marks the 1,000 m isobath. The “+” markers on top of the trajectories are 90 days apart. The colored dots indicate the seeding locations.

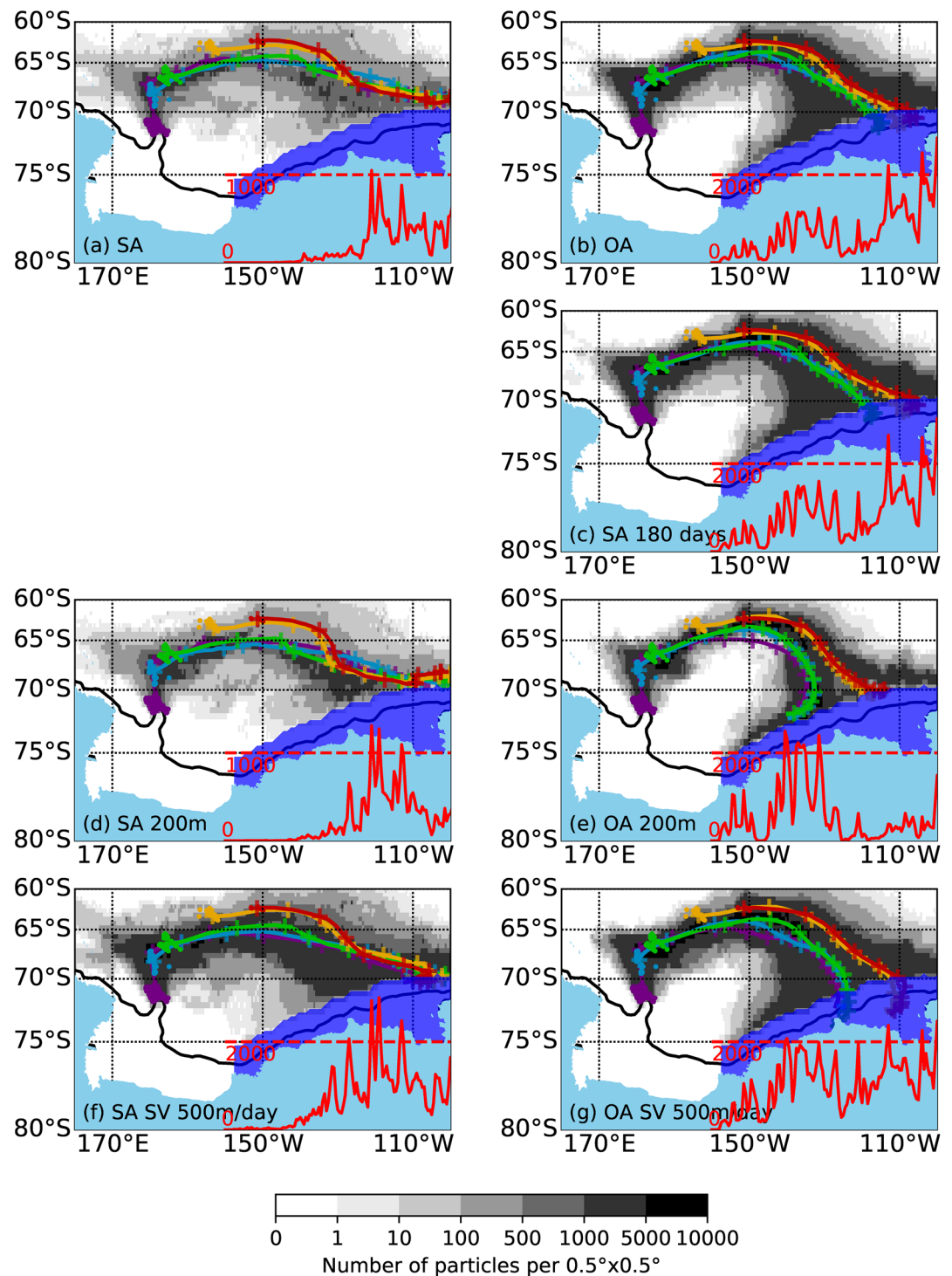


**Figure 5.** The same as Figure 4 but for successful particles. Successful particles are defined as particles that reach the target region (dark blue polygon) within 3 years of their release. Note the non-linear scale and particle trajectories have been truncated after they reached the target region. Solid lines represent the mean trajectories of the successful particles released from R1 (purple), R2 (light blue), R3 (green), R4 (orange), and R5 (red). The red lines indicate the number of particles which enter the target region at this longitude. (a) Sea-ice advection (SA); (b) Ocean advection (OA); (c) SA 180 days; (d) SA or OA at depth (200 m); (e) OA at depth (200 m); (f) SA + SV (500 m/day); (g) OA + SV (500 m/day). The black contour line marks the 1,000 m isobath. The “+” markers on top of the trajectories are 90 days apart. The colored dots indicate the seeding locations.

Ross Gyre but not advected far enough south into the target region. In addition, some particles from R1, R2, and R3 are entrained into the Balleny Gyre, to the west of the mean trajectory. In the OA scheme (Figure 4b), the mean pathways of R2–R5 for the unsuccessful particles are very similar to the sea-ice schemes but differs for particles from R1. In fact, more particles from R1 in the OA scheme enter the Balleny Gyre and continue within the Antarctic Slope Current further west. In addition to the elevated westward propagation, more particles are circling in the Ross Gyre compared to the sea-ice schemes. In the OA 200 m scheme (Figure 4e), the fraction of particles carried westward, particularly from R1, continues to increase and results in the distorted mean trajectory. In this scheme, more particles from R2 and R3 circulate in the Ross Gyre and do not leave the Ross Gyre like in the SA scheme. In both schemes with active swimming (Figures 4f and 4g), the trajectories show a slight southward shift compared to the schemes without active swimming. The SA 180 days scheme shows very similar results to the OA scheme.

Successful particles from the selected SA schemes all follow approximately the same trajectory (Figures 5a, 5d, and 5f). Over the first 100 days, the successful trajectories are very similar to the trajectories of the unsuccessful particles; however, the successful particles are then deflected southward and do not continue along the zonal path. After their southward deflection, the particles then veer to the east and enter the target region between 130 and 100°W. Only between 3% and 10% of particles enter the target region west of 130°W. The southward deflection of successful particles tends to occur further west for particles released from R1, whereas particles released from R4 and R5 change direction further to the east. Particles released at the southernmost release locations (R1 and R2) tend to follow a more direct route across the Ross Gyre toward the target region.

The distribution of successful particles from the selected OA schemes is more gradual (Figures 5b, 5e, and 5g) when approaching the target region compared to their SA counterparts. In the SA schemes, the spread, shown by the area which particles occupy, is larger and horizontal gradients smaller. On the other hand, OA particles enter the target region over a larger longitude range. Here the OA schemes show a larger number of particles to enter the target region west of 130°W compared to the SA schemes. This is particularly evident in the advection at depth scheme (Figure 5e). The trajectories of successful particles from the OA schemes seeded from R4 and R5 are similar to those from the SA schemes. However, after turning southward, the successful particles from the OA schemes continue to the target region along a more southward trajectory compared to a more eastward pathway of the SA schemes. The trajectories from R1 to R3 reach around 1° further north compared to the sea-ice advected particles. The particle flux into the target region and the mean trajectories suggest a separation into two clusters, a cluster where particles enter east and a cluster where particles enter west of 130°W. Particles from R1 to R3 account for most of the western cluster, while particles from R4 and R5 show a preference for the eastern cluster. Results from the SA 180 days scheme are similar to OA, but show higher particle influxes in the target region, as suggested by the overall higher recruitment success rate.

### 3.3. Variations in the Particle Arrival Age and Particle Influx Into the Target Region

Particles seeded closer to the target region reach the target region earlier, with timings of the first arrival very similar for sea-ice advected particles versus ocean advected particles (Figure 6). The influx of particles from the SA schemes shows a bimodal distribution with a higher influx than OA schemes. The bimodal peaks in the SA schemes are a year apart and occur during winter season, which suggests that sea-ice drift close to the target region causes the larger influx of particles during that period. The consequence of the lower but more continuous influx in the OA schemes is that, averaged over all particles, the arrival time in the OA schemes, is around 100 days longer. In the SA schemes the influx of particles decreases after 800 days while in the OA that occurs only after 1,000 days. Little change is seen between SA and SA 200 m (Figures 6a and 6d) while the influx of particles in OA 200 m up until 600 days (Figure 6e) is reduced compared to OA. Here, advection at depth delays the arrival of particles. In contrast, particles in schemes with active swimming arrive around 20 days earlier in the target region. The influx of particles into the target region and the arrival times from the SA 180 days scheme are very similar to that from the OA schemes.

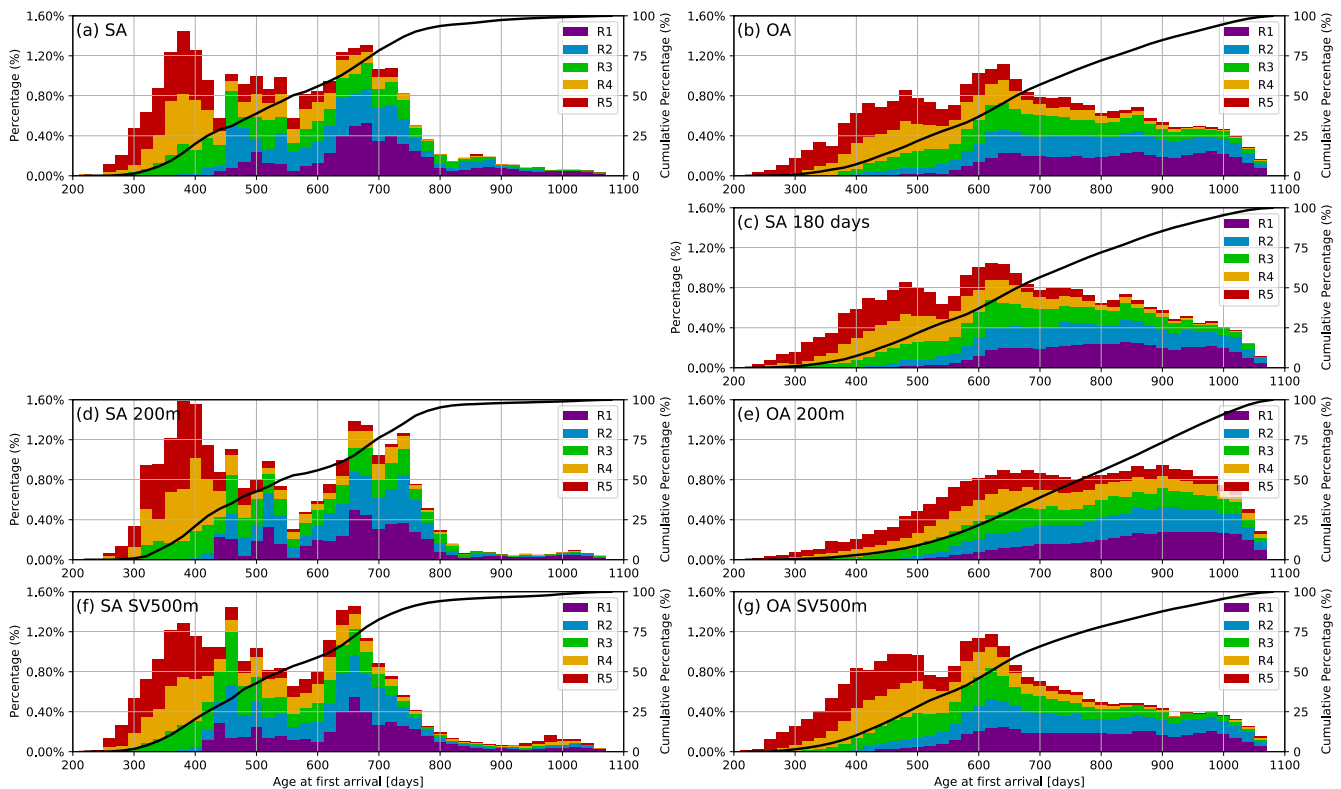


**Figure 6.** The age at first arrival for successful particles from selected sea-ice (SA) and ocean advection (OA) schemes versus influx rate (%). The area under the color shaded area is 100%. (a) Sea-ice advection (SA), (b) OA, (c) SA 180 days, (d) SA or advection at 200 m, (e) OA at 200m, (f) SA and active swimming of 500 m/day, and (g) OA and active swimming of 500 m/day. Age bins are 20 days apart. The color-coding represents the contribution from the individual release regions. The black line shows the cumulative percentage of particles which have reached the target region.

#### 4. Discussion and Conclusion

The current knowledge about the early life history of Antarctic toothfish (*D. mawsoni*) life cycle is limited, and several key questions are still not fully understood: How do eggs and juveniles manage to get from the known spawning grounds to the shelf region? What role does sea-ice drift and ocean currents play?

This article used a number of different advection schemes to investigate how potential spawning grounds could be connected to the shelf regions where the juvenile toothfish are found. The results from this study provide some insights about the recruitment success for certain spawning regions and how that is influenced by sea-ice drift and ocean currents. Incorporating sea-ice drift in such a connectivity study is novel and could be of importance to other species. In addition, the potential role of juvenile behavior impacting the recruitment success was investigated. While this paper covers a large set of schemes, it could not explore all the variability within a scheme and other possible schemes. As our knowledge advances with time, these scenarios will be revised, refined, and even potentially falsified.

Tracking the juveniles into adulthood was not carried out because there is scarce information when and if toothfish become bottom dwelling (e.g., see the discussions and modeling in Ashford et al., 2017). Similarly, restrictions apply to Patagonian toothfish and Lagrangian modeling studies have not progressed beyond the recruitment stage yet (Mori et al., 2016). The relatively high horizontal and vertical resolution of the ROAM15 grid (but presently without tides and the Ross Ice Shelf) suggests that we could continue to track toothfish development onto and then presumably off the Ross Sea continental shelf as they mature, potentially enabling a complete hypothetical life history using the model hydrodynamics, and particle tracking. This comes with caveats and challenges (Abrams et al., 2021) and as before, more complete toothfish life cycle observational data would make testing such juvenile to adult toothfish tracking more tractable.

The particle tracking presented here uses hydrodynamic data from a high-resolution ocean model, ROAM15. The fine model mesh of ROAM15 allows for mesoscale eddies to be explicitly resolved, while in coarser models parameterizations are used to incorporate the effect of mesoscale eddies (Gent & McWilliams, 1990). Alternatively, some Lagrangian studies incorporate a “random walk” to introduce additional diffusivity to account for unresolved processes (Faillettaz et al., 2018; Huret et al., 2010; Siegel et al., 2003). The modeled sea surface height, a measure for the geostrophic flow (Behrens et al., 2020; Mori et al., 2016), and sea-ice drift compares well to observations, which is essential for Lagrangian studies (Van Sebille et al., 2018). However, there are model biases in both ocean circulation and sea-ice drift which will impact the dispersal of particles. For example, observed sea-ice drifts along the northern Ross Gyre show a more northward directed drift while the modeled sea-ice drift suggests a more eastward direction. Therefore, particles advected with the observed fields would be carried into the Antarctic Circumpolar Current while particles based on the modeled field would stay closer to the Antarctic coast, which increases their recruitment success potential. Some uncertainties also exist around the observational datasets because measuring sea-surface height during winter, when sea-ice is present, is difficult (Armitage et al., 2018; Kwok & Morrison, 2015). On the other hand, the large number of released particles and a release period over consecutive years (2002–2016) will act to reduce some of the model uncertainties and increase confidence in the model results, since averaging statistics could be applied.

A diagnostic which measures the recruitment success rate of particle arrival at the continental shelf between the Ross and Amundsen Sea was used to argue that some juvenile behaviors (OA schemes and/or schemes with active swimming) are more beneficial for recruitment to the toothfish population in the Ross Sea. However, even very small recruitment success rates, as estimated for particles advected with sea-ice drift (~7%), could be sufficient to sustain a stable population (Cowen et al., 2006). The conducted simulations revealed that sea-ice advected particles reach the target region on average around 100 days earlier than ocean advected particles. This poses potentially an advantage against ocean advected particles, which exposes juveniles to open ocean predators for longer. However, SA schemes without active swimming showed intermittent recruitment success for certain years, which would be disadvantageous for a stable population. This suggests that juveniles transported with sea-ice drift require an additional behavior change to successfully reach the target region every year.

Observations and model results from the hindcast (Figure 1) show a coherent pattern regarding sea-ice drift in the northern and eastern Ross Gyre, where sea-ice drift is directed away from the target region. When juveniles pass through this region and follow the sea-ice drift they are likely to be carried away from the target region into the open ocean. It is therefore concluded—despite uncertainties around the modeling—that sea-ice drift in this region reduces the recruitment success. Modeled particles typically pass through this region and experience these conditions during their second winter season. However, the modeling has shown that a southward swimming or using ocean currents instead of sea-ice drift could mitigate this issue. Here, the simulation which used ocean currents after 180 days, before the onset of second winter season, showed a recruitment success rate of 29% compared to 7% if particles would continue following the sea-ice drift.

The modeling results show that the recruitment success rate is sensitive to the spatial extent of the target region. A very general and inclusive approach has been used in this study to define a “target region” comprising the shelf region between the eastern Ross and Amundsen Sea based only on the locations of the smallest (and therefore youngest) toothfish observed in fishery data (Hanchet et al., 2015). The recruitment success rates and related pathways change if the target region is modified; a target region located further north leads to generally higher recruitment success rates due to the recirculation of particles in the Ross Gyre; a more southern target region reduces the overall success rate accordingly. The change in the overall recruitment success rate is spread relatively evenly over the different seeding regions. Restricting the region further to the east of 155°W leads to a reduction in the overall recruitment success rates, evenly spread over all seeding regions. We outline the fact that the eastern extension of the target region is limited by the boundary of the nested model domain, which lies at 95°W. In addition, settling regions further west of the spawning region, around the Balleny Islands and west of it, have also been identified. However, this settling process has not been explored further due to the proximity to the target region, hampering the ability to link certain larval behavior, and recruitment success.

The presented recruitment success rates are only based on dispersal by physical variables using particles with some simple assumed behaviors. Juveniles in the real ocean are affected by additional factors, which have been neglected, but will impact the survival. One missing aspect is the food availability (Fiksen & Jorgensen, 2011) for the larvae and juveniles during their journey, which depends on various bio-physical properties (e.g., temperature, chlorophyll-a concentration, and zooplankton abundance) and varies in space and time. This is one of the proposed benefits of sea-ice, as the productivity derived from melting sea-ice (Duprat et al., 2016, 2020; Eicken, 1992) could provide a predictable and rich food source for juveniles. It is possible that the higher recruitment success rates with ocean advected particles could be impacted and reduced by lower food availability and longer exposure to open ocean predators. Reaching the target region early could be beneficial since the continental shelf could provide a rich food source and shelter. Also, the advection schemes with active swimming and DVM did not take into account the additional energy required in this process, which could lead to reduced recruitment success rates in reality. The advection schemes with DVM used here perform a repetitive 12-h cycle between surface and a given depth, but at these high latitudes there is a large seasonal cycle in daylight length. In which way this simplification affects the results is unknown and should be considered in future studies. However, it remains still unknown whether toothfish execute a form of DVM and how DVM is impacted by polar nights (Berge et al., 2009).

In conclusion, results of the SA schemes without active swimming challenge the current hypotheses on the juvenile toothfish life cycle, where the dispersal throughout egg and juvenile phase is thought to be highly associated with sea-ice drift. The low and intermittent recruitment success in these advection schemes promotes a behavior change after the eggs hatch, disconnected from passively drifting with sea-ice. In particular the sea-ice drift in the northern and eastern Ross Gyre during the second winter season, away from the Antarctic shelf, reduces the recruitment success. Instead, using ocean currents or actively swim toward the Antarctic shelf could offset this effect. Furthermore, a future decline of sea-ice in this region, might have only a limited impact on the toothfish recruitment success, since more ice-free conditions tend to result in higher recruitment success. In addition, observations of larvae and juvenile toothfish vertical distribution and swimming abilities would greatly improve the ability to model the trajectories and reconfirm our findings. Results of this study show a high sensitivity of the recruitment success to their behavior during that phase. An overall improved understanding about Antarctic toothfish early life history is essential for developing accurate population dynamics models used to ensure a sustainable fishery and also has implications for the effectiveness of the Ross Sea Marine protected area, which includes areas designated to protect key spawning locations, and locations to protect key juvenile recruitment and migration corridors.

### Data Availability Statement

Model and trajectory data can be freely obtained via <https://doi.org/10.5281/zenodo.4570967>, <https://doi.org/10.5281/zenodo.4574388>, and <https://doi.org/10.5281/zenodo.4574418>.

### Acknowledgments

This project obtained funding from Ministry for Business Innovation and Employment via C01X1710 Ross Ramp and C01X1902 Deep South National Science Challenge. We would like to thank the four reviewers whose comments and thoughts helped us to strengthen this study. We acknowledge the support of NeSI High Performance Computing Facility and its team. Finally, I would like to acknowledge my partner, son, and daughter.

### References

- Abras, A., García-Marin, J.-L., Heras, S., Vera, M., Agulló, M., Planella, L., & Roldán, M. I. (2021). Male deep-sea shrimps *Aristeus antennatus* at fishing grounds: Growth and first evaluation of recruitment by multilocus genotyping. *Life*, 11(2), 116.
- Armitage, T. W. K., Kwok, R., Thompson, A. F., & Cunningham, G. (2018). Dynamic topography and sea level anomalies of the southern ocean: Variability and teleconnections. *Journal of Geophysical Research: Oceans*, 123(1), 613–630. <https://doi.org/10.1002/2017jc013534>
- Ashford, J., Dinniman, M., & Brooks, C. (2017). Physical-biological interactions influencing large toothfish over the Ross Sea shelf. *Antarctic Science*, 29(6), 487–497. <https://doi.org/10.1017/s0954102017000359>
- Ashford, J., Dinniman, M., Brooks, C., Andrews, A. H., Hofmann, E., Cailliet, G., et al. (2012). Does large-scale ocean circulation structure life history connectivity in Antarctic toothfish (*Dissostichus mawsoni*)? *Canadian Journal of Fisheries and Aquatic Sciences*, 69(12), 1903–1919.
- Barnier, B., Madec, G., Penduff, T., Molines, J.-M., Treguier, A.-M., Le Sommer, J., et al. (2006). Impact of partial steps and momentum advection schemes in a global ocean circulation model at eddy-permitting resolution. *Ocean Dynamics*, 56(5–6), 543–567. <https://doi.org/10.1007/s10236-006-0082-1>
- Behrens, E., Fernandez, D., & Sutton, P. (2019). Meridional oceanic heat transport influences marine heatwaves in the Tasman Sea on interannual to decadal timescales. *Frontiers in Marine Science*, 6, 228. <https://doi.org/10.3389/FMARS.2019.00228>
- Behrens, E., Rickard, G., Morgenstern, O., Martin, T., Osprey, A., & Joshi, M. (2016). Southern Ocean deep convection in global climate models: A driver for variability of subpolar gyres and Drake Passage transport on decadal timescales. *Journal of Geophysical Research: Oceans*, 121(6), 3905–3925. <https://doi.org/10.1002/2015JC011286>

- Behrens, E., Williams, J., Morgenstern, O., Sutton, P., Rickard, G., & Williams, M. J. M. (2020). Local grid refinement in New Zealand's Earth system model: Tasman Sea ocean circulation improvements and Super-Gyre circulation implications. *Journal of Advances in Modeling Earth Systems*, 12(7). <https://doi.org/10.1029/2019MS001996>
- Berge, J., Cottier, F., Last, K. S., Varpe, Ø., Leu, E., Soreide, J., et al. (2009). Diel vertical migration of Arctic zooplankton during the polar night. *Biology Letters*, 5(1), 69–72. <https://doi.org/10.1098/rsbl.2008.0484>
- Carter, L., McCave, I., & Williams, M. J. (2008). Circulation and water masses of the Southern Ocean: A review. *Developments in Earth and Environmental Sciences*, 8, 85–114.
- Cowen, R. K., Paris, C. B., & Srinivasan, A. (2006). Scaling of connectivity in marine populations. *Science*, 311(5760), 522–527.
- Daher, H., Beal, L. M., & Schwarzkopf, F. U. (2020). A new improved estimation of Agulhas leakage using observations and simulations of lagrangian floats and drifters. *Journal of Geophysical Research: Oceans*, 125(4), e2019JC015753. <https://doi.org/10.1029/2019JC015753>
- Debreu, L., Vouland, C., & Blayo, E. (2008). AGRIF: Adaptive grid refinement in Fortran. *Computers & Geosciences*, 34(1), 8–13. <https://doi.org/10.1016/j.cageo.2007.01.009>
- Delandmeter, P., & van Sebille, E. (2019). The Parcels v2.0 Lagrangian framework: New field interpolation schemes. *Geoscientific Model Development*, 12(8), 3571–3584. <https://doi.org/10.5194/gmd-12-3571-2019>
- Dotto, T. S., Garabato, A. N., Bacon, S., Tsamados, M., Holland, P. R., Hooley, J., et al. (2018). Variability of the Ross Gyre, Southern Ocean: Drivers and responses revealed by satellite altimetry. *Geophysical Research Letters*, 45(12), 6195–6204. <https://doi.org/10.1029/2018gl078607>
- Duprat, L., Bigg, G. R., & Wilton, D. J. (2016). Enhanced Southern Ocean marine productivity due to fertilization by giant icebergs. *Nature Geoscience*, 9(3), 219–221. <https://doi.org/10.1038/ngeo2633>
- Duprat, L., Corkill, M., Genovese, C., Townsend, A. T., Moreau, S., Meiners, K. M., & Lannuzel, D. (2020). Nutrient distribution in East Antarctic Summer Sea Ice: A potential iron contribution from glacial basal melt. *Journal of Geophysical Research: Oceans*, 125(12), e2020JC016130. <https://doi.org/10.1029/2020JC016130>
- Eicken, H. (1992). The role of sea ice in structuring Antarctic ecosystems. *Polar Biology*, 12(1), 3–13.
- Faillietaz, R., Paris, C. B., & Irissou, J.-O. (2018). Larval fish swimming behavior alters dispersal patterns from marine protected areas in the North-Western Mediterranean Sea. *Frontiers in Marine Science*, 5(97). <https://doi.org/10.3389/fmars.2018.00097>
- Fichefet, T., & Maqueda, M. A. M. (1997). Sensitivity of a global sea ice model to the treatment of ice thermodynamics and dynamics. *Journal of Geophysical Research*, 102(C6), 12609–12646. <https://doi.org/10.1029/97JC00480>
- Fiksen, O., & Jorgensen, C. (2011). Model of optimal behaviour in fish larvae predicts that food availability determines survival, but not growth. *Marine Ecology Progress Series*, 432, 207–219. <https://doi.org/10.3354/meps09148>
- Gent, P. R., & McWilliams, J. C. (1990). Isopycnal mixing in ocean circulation models. *Journal of Physical Oceanography*, 20(1), 150–155. [https://doi.org/10.1175/1520-0485\(1990\)020<0150:IMIOCM>2.0.CO;2](https://doi.org/10.1175/1520-0485(1990)020<0150:IMIOCM>2.0.CO;2)
- Good, S. A., Martin, M. J., & Rayner, N. A. (2013). EN4: Quality controlled ocean temperature and salinity profiles and monthly objective analyses with uncertainty estimates. *Journal of Geophysical Research: Oceans*, 118(12), 6704–6716. <https://doi.org/10.1002/2013JC009067>
- Gouretski, V. (1999). The large-scale thermohaline structure of the Ross Gyre. In S. M. Spezie, & M. R. Manzella, (Eds.), *Oceanography of the Ross Sea Antarctica* (pp. 77–100). Springer. [https://doi.org/10.1007/978-88-470-2250-8\\_6](https://doi.org/10.1007/978-88-470-2250-8_6)
- Hanchet, S. M., Dunn, A., Parker, S., Horn, P., Stevens, D., & Mormede, S. (2015). The Antarctic toothfish (*Dissostichus mawsoni*): Biology, ecology, and life history in the Ross Sea region. *Hydrobiologia*, 761(1), 397–414. <https://doi.org/10.1007/s10750-015-2435-6>
- Hanchet, S. M., Rickard, G. J., Fenaughty, J. M., Dunn, A., Williams, M. J. H., Hanchet, et al. (2008). A hypothetical life cycle for Antarctic toothfish (*Dissostichus mawsoni*) in the Ross Sea region. *CCAMLR Science*, 15, 35–53.
- Huret, M., Petitgas, P., & Woillez, M. (2010). Dispersal kernels and their drivers captured with a hydrodynamic model and spatial indices: A case study on anchovy (*Engraulis encrasicolus*) early life stages in the Bay of Biscay. *Progress in Oceanography*, 57(1–4), 6–17.
- Kwok, R., & Morison, J. (2015). Sea surface height and dynamic topography of the ice-covered oceans from CryoSat-2: 2011–2014. *Journal of Geophysical Research: Oceans*, 121(1). <https://doi.org/10.1002/2015JC011357>
- La Mesa, M. (2007). The utility of otolith microstructure in determining the timing and position of the first annulus in juvenile Antarctic toothfish (*Dissostichus mawsoni*) from the South Shetland Islands. *Polar Biology*, 30(10), 1219–1226.
- Madec, G., Bourdallé-Badie, R., Bouttier, P.-A., Bruciaferri, D., Calvert, D., et al. (2017). *NEMO ocean engine*. Notes Du Pôle De Modélisation De L'institut Pierre-Simon Laplace.
- Meijers, A. J. S. (2014). The Southern Ocean in the Coupled Model Intercomparison Project phase 5. *Philosophical Transactions of the Royal Society A: Mathematical, Physical, and Engineering Sciences*, 372, 20130296. <https://doi.org/10.1098/rsta.2013.0296>
- Mori, M., Corney, S. P., Melbourne-Thomas, J., Welsford, D. C., Klockner, A., & Ziegler, P. E. (2016). Using satellite altimetry to inform hypotheses of transport of early life stage of Patagonian toothfish on the Kerguelen Plateau. *Ecological Modelling*, 340, 45–56.
- Mujica, A., Penailillo, D., Reyes, A., & Nava, M. L. (2016). Embryonic and larval development of *Dissostichus eleginoides* (Pisces: Nototheniidae). *Revista de Biología Marina y Oceanografía*, 51(3), 675–680. <https://doi.org/10.4067/S0718-19572016000300018>
- Orsi, A. H., & Wiederwohl, C. L. (2009). A recount of Ross Sea waters. *Deep-Sea Research Part II*, 56(13–14), 778–795. <https://doi.org/10.1016/j.dsr2.2008.10.033>
- Parker, S. J., & Di Blasi, D. (2020). *Second winter survey of Antarctic toothfish (Dissostichus mawsoni) in the Ross Sea region*. Commission for the Conservation of Antarctic Marine Living Resources, SC-CAMLR-39/BG/29.
- Parker, S. J., Stevens, D. W., Ghigliotti, L., La Mesa, M., Di Blasi, D., & Vacchi, M. (2019). Winter spawning of Antarctic toothfish *Dissostichus mawsoni* in the Ross Sea region. *Antarctic Science*, 31(5), 243–253. <https://doi.org/10.1017/S0954102019000282>
- Parker, S. J., Sundby, S., Stevens, D., Di Blasi, D., Schiaparelli, S., & Ghigliotti, L. (2021). *Buoyancy of post-fertilized Dissostichus mawsoni* eggs and implications for early life history. *Fisheries Oceanography*.
- Roach, C. J., & Speer, K. (2019). Exchange of water between the Ross Gyre and ACC assessed by lagrangian particle tracking. *Journal of Geophysical Research: Oceans*, 124(7), 4631–4643. <https://doi.org/10.1029/2018jc014845>
- Roberts, J. O. (2012). *Ecology and management of range edge populations: The case of toothfish species at the South Sandwich Islands*. Retrieved from <https://spiral.imperial.ac.uk/handle/10044/1/9969>
- Shaffrey, L., Stevens, I., Norton, W., Roberts, M., Vidale, P.-L., Harle, J., et al. (2009). UK HiGEM: The new UK high-resolution global environment model—Model description and basic evaluation. *Journal of Climate*, 22(8), 1861–1896.
- Siegel, D., Kinlan, B., Gaylord, B., & Gaines, S. (2003). Lagrangian descriptions of marine larval dispersion. *Marine Ecology Progress Series*, 260, 83–96.
- Sokolov, S., & Rintoul, S. R. (2009). Circumpolar structure and distribution of the Antarctic circumpolar current fronts: 2. Variability and relationship to sea surface height. *Journal of Geophysical Research: Oceans*, 114(C11), C11019. <https://doi.org/10.1029/2008jc005248>

- Thompson, A. F., Stewart, A. L., Spence, P., & Heywood, K. J. (2018). The Antarctic slope current in a changing climate. *Reviews of Geophysics*, *56*(4), 741–770. <https://doi.org/10.1029/2018rg000624>
- Tsujino, H., Urakawa, S., Nakano, H., Small, R. J., Kim, W. M., Yeager, S. G., et al. (2018). JRA-55 based surface dataset for driving ocean–sea-ice models (JRA55-do). *Ocean Modelling*, *130*, 79–139. <https://doi.org/10.1016/j.ocemod.2018.07.002>
- Van Sebille, E., Griffies, S. M., Abernathey, R., Adams, T. P., Berloff, P., Biastoch, A., et al. (2018). Lagrangian ocean analysis: Fundamentals and practices. *Ocean Modelling*, *121*, 49–75.